Myllys, M.; Maunuksela, J.; Alava, M.; Ala-Nissila, T.; Merikoski, J.; Timonen, J.

Kinetic Roughening in Slow Combustion of Paper

Kinetic roughening in slow combustion of paper

M. Myllys,[1] J. Maunuksela,[1] M. Alava,[2] T. Ala-Nissila,[2,3] J. Merikoski,[1] and J. Timonen[1]

[1]*Department of Physics, University of Jyväskylä, P.O. Box 35, FIN-40351 Jyväskylä, Finland*
[2]*Laboratory of Physics, Helsinki University of Technology, P.O. Box 1100, FIN-02015 HUT, Espoo, Finland*
[3]*Helsinki Institute of Physics, P.O. Box 9 (Siltavuorenpenger 20 C), FIN-00014 University of Helsinki, Helsinki, Finland*
and Department of Physics, Brown University, Providence, Rhode Island 02912-1843

Results of experiments on the dynamics and kinetic roughening of one-dimensional slow-combustion fronts in three grades of paper are reported. Extensive averaging of the data allows a detailed analysis of the spatial and temporal development of the interface fluctuations. The asymptotic scaling properties, on long length and time scales, are well described by the Kardar-Parisi-Zhang (KPZ) equation with short-range, uncorrelated noise. To obtain a more detailed picture of the strong-coupling fixed point, characteristic of the KPZ universality class, universal amplitude ratios, and the universal coupling constant are computed from the data and found to be in good agreement with theory. Below the spatial and temporal scales at which a crossover takes place to the standard KPZ behavior, the fronts display higher apparent exponents and apparent multiscaling. In this regime the interface velocities are spatially and temporally correlated, and the distribution of the magnitudes of the effective noise has a power-law tail. The relation of the observed short-range behavior and the noise as determined from the local velocity fluctuations is discussed.

I. INTRODUCTION

The phenomenon of kinetic roughening of driven fronts is abundant in nature. It has also become one of the paradigms in the physics of nonequilibrium systems. The theoretical interest arises since, as in critical equilibrium systems, the roughening behavior can be understood in terms of scaling exponents and scaling functions [1–3]. A classification of kinetic roughening phenomena can be obtained by mapping the dynamics to an appropriate Langevin equation that describes the interface dynamics, and also includes a noise term with system specific correlations and magnitude distribution.

The simplest nonlinear interface equation related to kinetic roughening is the celebrated Kardar-Parisi-Zhang (KPZ) equation [4], also related to the Burgers' equation of hydrodynamics. The KPZ equation for a growing surface can be expressed in the form

$$\frac{\partial h(x,t)}{\partial t} = \nu \frac{\partial^2 h(x,t)}{\partial x^2} + \frac{\lambda}{2}\left[\frac{\partial h(x,t)}{\partial x}\right]^2 + F + \eta, \quad (1)$$

where $h(x,t)$ is the height of the interface, F is the driving force, and η denotes the noise affecting the interface. In the case η is short-range correlated in time and space, it can be substituted asymptotically by white, thermal (Gaussian) noise: $\langle \eta(x,t)\rangle = 0$ and $\langle \eta(x,t)\eta(x',t')\rangle = 2D\,\delta(x-x')\,\delta(t-t')$. The KPZ equation contains a linear diffusion term that imposes a surface tension through ν, and the nonlinearity is proportional to λ. The essential physics of the KPZ universality class arises from the presence of additional symmetries, in particular a nonzero growth velocity component in the direction perpendicular to the local surface orientation.

The scaling properties as implied by the KPZ equation can be discussed starting from, e.g., the Family-Vicsek scaling [5]. It establishes a scaling relation for the surface width $w^2(L,t) \equiv \overline{\langle (h-\bar{h})^2\rangle}$ as a function of time t and system size L, such that

$$w^2(t) = t^{2\beta} f(t/L^z) \propto \begin{cases} t^{2\beta} & \text{for } \xi \ll L \\ L^{2\chi} & \text{for } \xi \gg L. \end{cases} \quad (2)$$

Here $\xi \sim t^{1/z}$ denotes a correlation length, which increases with time until the finite system size induces a saturation. The overbar and brackets denote spatial and noise averaging, respectively. Meanwhile three exponents have been defined: the growth (β) and roughness (χ) exponents, and the dynamical exponent $z = \chi/\beta$. For the KPZ equation with white noise ("thermal" KPZ or TKPZ), the exponents can be established exactly in one spatial dimension, and are $\beta = 1/3$, $\chi = 1/2$, and $z = 3/2$ [6,4].

The TKPZ universality class is distinguished not only by the scaling exponents but also by other characteristic properties. The *scaling function* $f(x)$ of Eq. (2) is another landmark of the KPZ equation [4,6–9]. In the steady state the KPZ interfaces are in fact equivalent to random walks, since a fluctuation-dissipation theorem exists in $(1+1)$ dimensions, depending only on the effective noise strength and surface tension, but not on λ. On the other hand, temporal fluctuations on short time scales, and transient phenomena, do depend on the nonlinearity. Thus the scaling function $f(x)$ and its properties provide a distinct confirmation of the TKPZ roughening.

Consider the spatial (x') and temporal (t') two-point function of the interface fluctuations $\delta h(x,t)$ around the mean interface $\bar{h}(t)$

$$C_2(r,t) = \langle \overline{[\delta h(x',t') - \delta h(x'+r,t'+t)]^2}\rangle_{x',t'}. \quad (3)$$

The equal-time limit $t = t'$ defines $G_2(r)$, and for the (T)KPZ universality class we have

$$G_2(r) \approx A r^{2\chi}. \tag{4}$$

Here A denotes an amplitude that depends [2] on the parameters of the KPZ equation Eq. (1), $A = D/\nu$. Since this amplitude describes the steady-state fluctuations, it is related to the saturation width, and one finds [10–12] that $w_{sat} = (A/12)^{1/2} L^{\chi}$. Likewise, for the temporal correlation function, defined through Eq. (3) by taking $r = 0$, we have [8,10–12]

$$C_{s,2}(t) \approx B t^{2\beta}, \tag{5}$$

where $B = |\lambda|^{2\beta} A^{\beta+1} R_G$ denotes a dynamical amplitude and includes a universal constant R_G that characterizes the universality class of the system. Notice that B depends on λ, signaling that $C_{s,2}$ is related to the transient interface properties. R_G can thus be determined as a *universal amplitude ratio*, $R_G = B/(|\lambda|^{2\beta} A^{\beta+1})$. Other similar amplitude ratios can also be defined [2]. The values of R_G, as obtained [8,10–12] from mode-coupling theory and simulations, are in the range $R_G = 0.63$–0.71. The correlation functions can as well be used to determine the *universal coupling constant* [8] such that

$$g^* = \frac{\lambda}{2} \left[\frac{A}{B^{z/2}} \right]^{1/\chi}. \tag{6}$$

Hwa and Frey have obtained [8] the value $g^* \simeq 0.87$ based on a mode-coupling solution of the $(1+1)$-dimensional TKPZ problem. This calculation was later revised, and put in a more systematic form [13] (see also [9]), and compares well with the results from numerical studies of the scaling function [12,10].

Thus there are two distinct goals for an experimental study of interfaces, expected to be in the TKPZ universality class. The power-law behaviors of the bare interface correlations should enable an estimation of the exponents χ, β, and z. Then, by augmenting these data with a determination of λ, one can probe the scaling behavior beyond the scaling exponents by considering the universal amplitude ratios and, possibly, the scaling functions of the fluctuations. Experimentally, the issue is complicated by the existence of *crossovers* from short-range behaviors to the asymptotic TKPZ behavior, which would affect, e.g., the behavior of the height distribution, as compared to the pure TKPZ case. We have previously reported results on both the asymptotic scaling [14] and on the properties of the short-range (SR) regime [15]. In this paper our goal is to present a coherent picture of TKPZ physics in an experimental system, including more data and discussion related to the behavior at short scales. To this end, we have carried out additional high-resolution combustion-front experiments using very thin and light lens paper similar to that used in [16], in addition to our previous data [15] on two grades of ordinary copier paper, which are much thicker and heavier. The existence of large quantities of data allows us to do extensive averaging, typically over 10 000–40 000 interfaces. This is necessary to establish the correlation functions and their scaling properties reliably, in a complete analogy with numerical experiments. Our results establish, clearly, the existence of asymptotic TKPZ scaling in terms of the exponents. Moreover, we are able to determine the universal amplitude ratios and the fixed-point coupling constant in fair agreement with theoretical estimates.

The short-range behavior in an experimental system can differ from the asymptotic scaling because of three fundamental reasons. First, the effective interface equation may become TKPZ-like only *during coarse graining*. A case of this kind is provided by the Kuramoto-Sivashinsky equation [17], where TKPZ scaling can be found only at large enough scales. Second, irrelevant terms in the renormalization group sense, neglected in the KPZ equation, may produce [18] short-range effects. The third possibility is that, still within the experimentally accessible window of spatial and temporal scales, the effective noise η in Eq. (1) proves to be more complicated. Consider a slowly moving interface, in the proximity of a pinning/depinning transition that takes place at a critical F_c. Since the interface moves in a landscape with frozen-in or quenched inhomogeneities, η will depend on $h(x,t)$. For large enough driving forces, $F \gg F_c$, such noise correlations vanish. For intermediate F one can define a crossover length scale, above which the behavior and noise correlations are TKPZ-like. Below that scale, very close to F_c, the moving interface should have an effective $\beta \simeq \chi \simeq 0.75$ [19], accompanied by apparent multiscaling.

The correlations that arise from quenched noise can be generalized to temporal or spatial power-law correlations in the η [7,20] with the correlator $\langle \eta(x,t) \eta(x',t') \rangle = 2D\rho(x-x')\Delta(t-t')$. If the correlators ρ or Δ decay slowly enough, i.e., algebraically, the TKPZ exponents change [7]. The presence of cutoffs in the algebraic decay of ρ and Δ will induce again a crossover to the TKPZ scaling. Similarly, a power-law amplitude probability distribution function $P(\eta) \sim \eta^{-(1+\mu)}, \eta \geq 1$, can change the scaling behavior. For pure power laws, there is a critical value of $\mu_c \simeq 4$, below which the roughening behavior depends on μ. For $\mu = 3$, e.g., the qth order spatial two-point correlation functions have [15] short-range roughness exponents that change from about 0.76 ($q = 1$) to 0.15 ($q = 9$), while the asymptotic behavior is self-affine, with $\chi \simeq 0.76$ [21].

In the following we will therefore also elucidate the SR behavior, by looking at the noise in the slow-combustion experiments, and how the correlations of this noise and its amplitude distribution are reflected in the SR scaling. Many different experiments on surface growth, erosion, imbibition (paper wetting), fluid invasion, and also slow-combustion fronts in paper, have failed to demonstrate asymptotic TKPZ scaling, though one can of course ask whether all of these problems should be described by a local interface equation [22]. Exceptional fluctuations in the noise amplitude have been observed in fluid-flow experiments [23], and were reported earlier by us [15] for slow-combustion fronts. The roles of the crossover, also noted in fluid-flow experiments [24], and in penetrating magnetic flux fronts in thin-film superconductors [25], and of the effective noise in confusing the issue are to be noted. This may suffice as an explanation

as to why TKPZ behavior was not seen in the first similar experiment on slow-combustion front roughening [16] in contrast with our results.

Our impression is that in the slow-combustion fronts the SR physics largely arises from the presence of ''nonideal'' noise related to the quenched impurities in the burning material, and to the natural fluctuations due, e.g., to gas flow during the combustion process. We observe non-self-affine SR scaling, or multiscaling: the exponents χ and β depend on the order of the correlation function from which they are measured. A high local front velocity is naturally coupled to a local, steep interface gradient. At such locations the interface propagates faster, both parallel and perpendicular to the interface orientation, since λ is positive. In the SR regime the front dynamics is coupled to the nonstandard noise, which is both SR correlated and displays nontrivial amplitude fluctuations. The interplay of usual KPZ physics with the noise properties results in the absence of usual self-affine scaling. One of the origins of the quenched SR noise may lie in the local concentration variations of the potassium nitrate that is used to control the slow combustion. These experiments have been done at concentrations large enough to ensure that an eventual pinning regime is far away ($F \gg F_c$).

The paper begins in Sec. II with a detailed description of the high-resolution experimental setup. Section III is devoted to an analysis of the paper samples on which the experiments are done. In Sec. IV we present results for the scaling exponents for all three paper grades used in the experiments, starting with the asymptotic long-range limit and touching then on the short-range behavior. Noise correlations are studied in detail for the lens paper, and compared with those for the copier papers reported in Ref. [15]. Finally, we determine the universal amplitude ratios for all three experimental cases in the asymptotic regime. Section V comprises a discussion about implications of our results to theory and to other related experiments.

II. EXPERIMENTAL SETUP

The experimental setup shown as a schematic diagram in Fig. 1 consists of a combustion chamber, a camera system, and a computer with necessary hardware and software. One side of the combustion chamber is made of glass and the opposite side is a detachable aluminum plate for installing the paper samples. The rest of the chamber sides are lined with a layer of porous material 50 mm apart from the walls for making the incoming air flow laminar. In the middle of the chamber there is a detachable sample holder, designed for a maximum paper size of 600×400 mm^2. It can be rotated with respect to the adjustable air flow so that convective transfer of heat ahead of the propagation front can be regulated, and the other flow-dependent features can be optimized. The sample holder is an open metallic frame whose sides are both lined with needles that keep the paper sheet planar during combustion. If the extra heat losses at the boundaries need to be compensated for, the sides of the sample can be heated with filaments that follow the combustion front. The volume flow through the chamber was adjusted if necessary with an electrical fan, placed on top of the
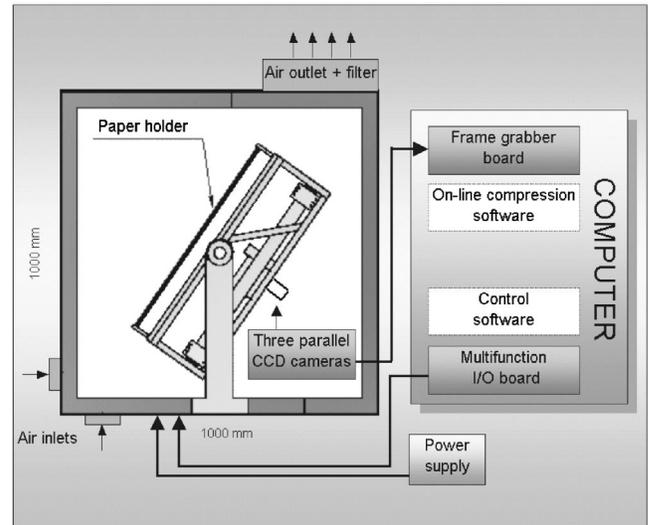

FIG. 1. A schematic diagram of the experimental setup.

chamber. The air flow through the chamber was also numerically simulated, and the velocity field around the sample was found to be quite homogeneous. To minimize the dissipation of heat from the combustion front, and to keep the air flow laminar, we used relatively low volume flows (approximately 20 l/s for the copier papers and no forced flow for the lens paper).

In the case the direction of air flow in the chamber was from bottom to top, combustion fronts were ignited from the top end of the paper samples by a tungsten heating wire in order to minimize convective heat transfer. In the original setup reported in [14], the recording of the front was done by a single charge-coupled device (CCD) camera, and the video signal was recorded on a Super-VHS recorder. In the present [15] setup, the propagating front was recorded with three parallel PULNiX TM-6EX black and white CCD cameras, whose images are composed of 768×548 pixels. The largest combined image contains 2304×548 pixels. Cameras were attached to a stand that was operated with a pneumatic cylinder. The camera system was automatically moved in regular intervals along the direction of propagation.

The digital frames of the three cameras were joined together and compressed online, and then recorded on a hard disk using a multilevel gray scale. The compressing of the frames was done by recording only a narrow stripe around the front line. Since recording was made in darkness, the only visible object was the combustion front. By omitting the dark background, we were able to reduce the size of the individual frame file from 431 kB to approximately 15 kB. The front height function was determined from each frame by first finding the pixels brighter than a given gray-scale value. A single-valued front line was fitted into the brightness profile in the strip found. In the intervals, where a front line could not be identified, a straight line was fitted by interpolation. The cylindrical image distortions caused by the lenses were corrected using nonlinear warping. The method needs a collection of two-dimensional landmark points whose true locations are known together with their distorted images. These were then used to define a global warping
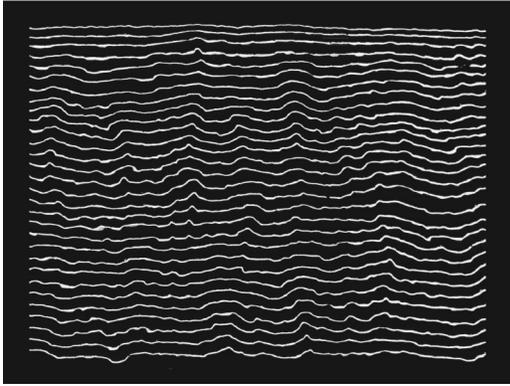
FIG. 2. Series of typical digitized fronts. The time step between successive fronts is 10 s, and the width of the digitized area is 310 mm.

function. Using this warping function, corrections were made into the position data of the individual cameras before joining them. A series of typical fronts from the experiments are shown in Fig. 2.

Improvements in data acquisition and introduction of the three-camera setup increased the temporal and spatial resolution of the equipment. For a 390-mm-wide and 500-mm-long paper sample, when the distance between the sample and the cameras was 70 mm, the instantaneous recorded area was 310×74 mm^2, and the pixel size was 0.135 mm. This was an order of magnitude below the maximum typical length scale related to areal mass variations in the paper samples, a few millimeters. It was also of the same order of magnitude, actually a bit smaller than the average width of the burning area in the combustion fronts, which sets the lower limit to details that can be detected. The maximum scanning frequency of the camera system was 10 frames per second. Since the average velocity of the fronts for the copier paper used in the present experiments was approximately 0.5 mm/s, it was sufficient to store only every second frame of the digitized fronts. During one time step, $\Delta t = 0.2$ s, the front propagated less than one pixel length. For the lens paper we had to slightly modify our experimental setup. Needles in paper holder were not suitable for attaching the thin paper, instead metallic bars were used on both sides. Combustion fronts were ignited from the bottom and every successive front was recorded because of their much higher average velocity (6–8 mm/s) compared to those in copier papers and, as noted already above, for the lens-paper samples we used no forced ventilation in the chamber. This kind of setup was similar to that in the early experiments reported in [16].

III. SAMPLES

The experiments were done using two different, easily available grades of copier paper, with basis weights of 70 gm^{-2} and 80 gm^{-2}, and very thin lens paper with a basis weight of 9.1 gm^{-2} [26]. It is important to realize that the composition of the paper has an impact on the propagation of the combustion front. Slow-combustion fronts do not easily propagate in a material made of pure cellulose fibers

only, because of their very low conductivity of heat. In normal copier papers approximately one-fourth of the basis weight is composed of fillers. In our case, the fillers in both grades of copier paper were mostly calcium carbonate (CaCO$_3$) with a high heat capacity, in comparison with cellulose, which improved the propagation of combustion fronts. In addition, potassium nitrate (KNO$_3$) was added as an oxygen source to all grades of paper to ensure a uniform propagation of slow-combustion fronts. The concentration of KNO$_3$ in the samples was kept at a value of approximately 0.8 gm^{-2}. Potassium nitrate was usually added by embedding the samples in an aqueous solution of KNO$_3$ for 5 min, after which they were dried in a press to maintain their planar shape. Due to the lower basis weight and much more porous structure of lens paper, drying of KNO$_3$ solution was not homogeneous over the sample, leading to an inhomogeneous concentration distribution of KNO$_3$. This would have a significant effect on the experiments, as will be discussed later. To avoid such problems, KNO$_3$ was added to lens-paper samples by spraying.

A second potential problem with paper samples is that it has been shown [27] that, especially for low basis-weight laboratory paper sheets, there may exist nontrivial power-law correlations in the basis weight that may extend up to about 15 times the fiber length, i.e., into the centimeter range. As it is well known [28] that correlated noise affects the scaling behavior of kinetic roughening, maps of the local mass variations were prepared for both grades of copier paper before and after the KNO$_3$ treatment. These β radiographs were taken from paper samples of size 170×90 mm^2 using spatial resolution of 0.04 mm. For the lens paper we used optically scanned images to estimate the local mass variations. In addition, we measured the calcium and potassium concentration distributions in several layers of the same samples using the laser-ablation method [29] with a spatial depth resolution of 0.2 mm.

The radiographs of the copier paper samples were analyzed using the two-point density fluctuation correlation function

$$C_m(\vec{r}) = \langle [m(\vec{x}) - \bar{m}][m(\vec{x} + \vec{r}) - \bar{m}] \rangle, \tag{7}$$

where $m(\vec{x})$ is the local areal mass or the local basis weight, $\bar{m}$ its average, and brackets denote an average over the sample. The results in Fig. 3 show that in both cases, after a distance of about 1 mm, a faster than algebraic (power-law) decay of correlations can be seen. This is in particular the case with the 70-gm^{-2} paper, while in the heavier paper samples the noise level is reached rapidly. We may conclude that addition of KNO$_3$ has not affected the basis-weight correlations. The basis-weight distributions $P(m) \equiv N(m)/\Sigma_{m'}N(m')$, where $N(m)$ is the number of locations with the same basis weight, differ from Gaussians only on the low basis-weight sides, which is most likely caused by rounding errors in the digitization of the β radiographs.

The results of the laser-ablation measurements were analyzed by a correlation function similar to that in Eq. (7). The difference was that, instead of the local basis weight, we used either the calcium or potassium atomic emission line
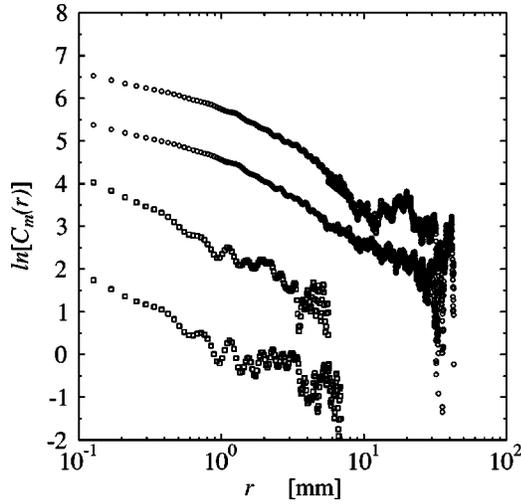
FIG. 3. A log-log plot of the correlation function $C_m(r)$ for four copier paper sheets of basis weights 70 gm^{-2}, 70 gm^{-2} treated with KNO_3, 80 gm^{-2}, and 80 gm^{-2} treated with KNO_3 (from top to bottom). The curves have been shifted vertically for clarity.

intensity, which is proportional to the vaporized mass. The intensity-fluctuation correlation functions were found to collapse to the noise level within a distance of 1 mm in every layer. After the KNO_3 treatment the mean potassium intensity was found to be greater for the 70 gm^{-2} than for the 80 gm^{-2} paper. In order to reach the same concentration of potassium nitrate for both grades, we used a stronger aqueous solution of KNO_3 for the heavier paper.

To summarize, the results indicate that there are no correlations in the filler, the local basis weight, or potassium nitrate distributions beyond a few millimeters, and that the structures of the samples are isotropic.

IV. KINETIC ROUGHENING OF SLOW-COMBUSTION FRONTS

A. Front width and correlation functions

The most straightforward way to estimate the scaling exponents β and χ for self-affine fronts is to use the scaling properties of the interface width $w(L,t)$, as mentioned in the Introduction. However, due to the large fluctuations in data when dealing with slow-combustion fronts, it is useful to consider the qth order two-point height-difference correlation functions

$$C_q(r,t) = \langle \overline{[\delta h(x',t') - \delta h(x'+r,t'+t)]^q} \rangle_{x',t'}, \quad (8)$$

where, again, $h(x,t)$ is the height of the front at point x and time t, and $\delta h(x,t) \equiv h(x,t) - \bar{h}(t)$, and the bar denotes an average over a front while the brackets denote an average over all configurations (fronts and burns). Through this quantity, one can define the two functions

$$G_q(r) \equiv C_q(r,0) \sim r^{\chi_q}, \quad (9)$$

and

$$C_{s,q}(t) \equiv C_q(0,t) \sim t^{\beta_q}, \quad (10)$$

which thus provide estimates for the roughness and growth exponents. In the saturated regime the functions $G_q(r)$ can be averaged over all times (steady-state configurations), and $C_{s,q}(t)$ over all spatial points.

Another quantity of interest for which fluctuations can be efficiently averaged out, is the *local* width of the propagating front $w(\ell,t)$, defined as

$$w^2(\ell,t) = \langle\langle[h(x,t) - \langle h(x,t)\rangle_\ell]^2\rangle_\ell\rangle, \quad (11)$$

where the notation $\langle\rangle_\ell$ denotes spatial averaging over all subsystems of size ℓ of a system of total size L. For growing self-affine interfaces, the scaling exponents satisfy $\beta_q = q\beta$ and $\chi_q = q\chi$, and the local width follows the Family-Vicsek scaling relation [5] given by

$$w^2(\ell,t) \sim \begin{cases} t^{2\beta} & \text{for } t \ll \ell^z \\ \ell^{2\chi} & \text{for } t \gg \ell^z. \end{cases} \quad (12)$$

This provides an another way to estimate the scaling exponents from experimental data.

B. Results for scaling exponents

1. Data analysis

In order to reduce the influence of boundary effects on the data, an area of width 270 mm taken in the middle of the recorded area of width 390 mm was used to calculate $h(x,t)$. The scaling exponents χ_q and β_q were then determined by performing a linear least-squares fit to the corresponding two-point height correlation functions [Eq. (8)] in the scaling regime. An *independent* estimate for the roughness exponent χ was obtained from the local width. The early-time behavior of the surface width [Eq. (11)] also gave an estimate for the growth exponent β. Accurate determination of the scaling exponents was complicated by the "intrinsic" width of the fronts caused also by random structural inhomogeneities of the samples. Therefore, in the spirit of the usual *convolution* ansatz [30–32] by which a random process affecting the front but independent of the front dynamics will induce an additive constant in the square of the front width, we performed linear least-squares analysis of $\log_{10}[G_q(2r) - G_q(r)] = q\chi \log_{10}(r) + \text{const}$, and of $\log_{10}[C_{s,q}(2t) - C_{s,q}(t)] = q\beta \log_{10}(t) + \text{const}$, to get rid of additive constant factors in the correlation functions. The results given in the text are obtained after these "intrinsic widths" were subtracted.

2. Roughness exponent χ

First, we present results for the roughness exponent χ_2 using the second-order correlation functions and the local width. The main results for both $\chi = \chi_2/2$ and $\beta = \beta_2/2$ are summarized in Tables I and II for all three paper grades. In the latter Table all the fits have been done by first subtracting the intrinsic widths from the data. The corresponding spatial correlation functions $G_2(r)$ are shown in Figs. 4 and 5 so that in the latter figure the intrinsic widths have been sub-

TABLE I. The scaling exponents β and χ, crossover values r_c and t_c, and average velocities.

	$C_2(r,t)$			$w(\ell,t)$		
	70 gm^{-2}	80 gm^{-2}	9.1 gm^{-2}	70 gm^{-2}	80 gm^{-2}	9.1 gm^{-2}
χ_{SR}	0.88(2)	0.89(2)	0.83(1)	0.81(6)	0.83(5)	0.81(1)
χ_{LR}	0.53(3)	0.51(3)	0.53(4)	0.57(1)	0.55(2)	0.56(2)
r_c(mm)	4.7(4)	6.0(5)	11(2)	12(7)	14(6)	18.8(4)
β_{SR}	0.59(4)	0.69(2)	0.61(2)			
β_{LR}	0.40(3)	0.39(3)	0.46(2)	0.29(3)	0.32(3)	0.28(5)
t_c(s)	25(9)	27(5)	3.7(4)			
v(mm/s)	0.64(2)	0.50(2)	9.0(5)			

tracted. It is immediately evident from the data that there are two regimes of apparent scaling, separated by a crossover length r_c. In the SR regime below the crossover length, $G_2(r)$ scales with a rather large effective exponent of $\chi_{SR} \simeq 0.90$ for the heavier paper grades, and 0.85 for the lens paper. In the long-range (LR) regime $r \gg r_c$, the effective exponent χ_{LR} converges very close to the exact KPZ value of 1/2 for all three cases. Beyond about 100 mm the statistics becomes worse and fluctuations larger. The inset in Fig. 5 shows estimates for the effective running exponents defined as $\chi_{\text{eff}} = (1/2)\log_{10}[\{G_2(2r_2) - G_2(r_2)\}/\{G_2(2r_1) - G_2(r_1)\}]/\log_{10}(r_2/r_1)$, where $r_2 = 4 r_1$. In all three cases, the LR asymptotic approach towards the TKPZ behavior is evident. It is also evident from this inset that no clear scaling regime can be found at short range with the higher apparent exponent. The behavior of the local width $w^2(\ell)$ averaged over the same data is consistent with $G_2(r)$ as is demonstrated in Fig. 6 where the intrinsic width is subtracted.

3. Growth exponent β

The temporal correlation functions $C_{2,s}(t)$ for the three cases are shown in Fig. 7 with the intrinsic widths removed. The poor time resolution ($\Delta t = 4.2$ s) in the 70-gm^{-2} paper data prevented us from analyzing in this case the temporal behavior very accurately. In the long-time regime the scaling behavior of the paper grades is again in agreement with the TKPZ case. The measured β_{LR} is, in particular after the intrinsic width has been removed, in good agreement with the TKPZ value 1/3. The largest deviations are shown by the lens paper as in this case the saturated regime was too short for an accurate determination of β. As was done in the case of the χ's, we also used the local width, Eq. (11), to compute the β_{LR}. The scaling range is in this case slightly less than a decade, and the exponents obtained (without subtracting the

intrinsic width) agree well with the TKPZ one. Note that the same data for $w(\ell,t)$ is used below to study its scaling function.

In the data, there is a crossover at time t_c from short-time behavior to asymptotic long-time regime visible in each case. The short-time growth exponent β_{SR} is, again, rather large, $\beta_{SR} = 0.75(5)$ for the 80-gm^{-2} case, and 0.64(3) for the lens paper. In the long-time regime beyond the crossover time, the exponent β_{LR} is again fully consistent with the TKPZ value of 1/3. The inset in Fig. 7 shows the approach of the effective running exponents $\beta_{\text{eff}} = (1/2)\log_{10}[\{C_{2,s}(2t_2) - C_{2,s}(t_2)\}/\{C_{2,s}(2t_1) - C_{2,s}(t_1)\}]/\log_{10}(t_2/t_1)$, where $t_2 = 4 t_1$, towards the TKPZ limit. Also in this case there is no clear scaling regime below the crossover time, although an apparent scaling exponent can be determined.

4. Multiscaling at short range

Spatial higher-order correlation functions, Eq. (8), were determined to check the possible multiscaling properties of the combustion fronts for the lens paper, to accompany the data published earlier [15] for the copier papers. The behavior of the higher-order correlation functions indicates that, in the TKPZ regime, the interfaces are self-affine. On the other hand, in the SR regime the slopes of the spatial and temporal correlation functions of Figs. 8 depend on the order q of the correlation function, i.e., show apparent multiscaling [33,34,21], similar to that found for the two grades of copier paper [15].

Analysis of the fitted SR scaling exponents reveals that the $\chi_{SR}(q)$'s approach the value 1/2 for large q, which means that larger local slopes follow a Gaussian distribution and are uncorrelated as in the long-range TKPZ regime. At the same time, $\beta_{SR}(q)$'s become very small and seem to approach zero. We conclude that the overall behavior of the SR

TABLE II. The scaling exponents β and χ obtained by first subtracting the intrinsic widths from the data.

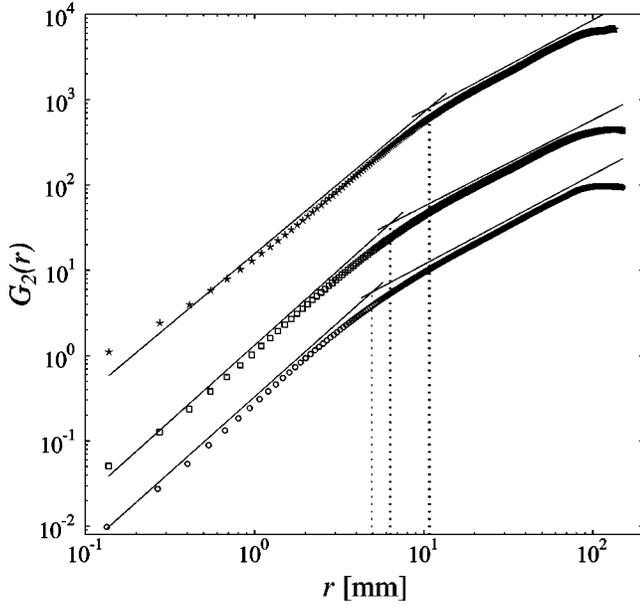|	$C_2(r,t)$			$w(\ell,t)$		
	70 gm^{-2}	80 gm^{-2}	9.1 gm^{-2}	70 gm^{-2}	80 gm^{-2}	9.1 gm^{-2}
χ_{SR}	0.90(3)	0.90(4)	0.85(1)	0.84(6)	0.87(8)	0.95(6)
χ_{LR}	0.50(4)	0.47(4)	0.50(6)	0.56(1)	0.52(5)	0.51(1)
β_{SR}		0.75(5)	0.64(3)			
β_{LR}	0.36(3)	0.34(4)	0.43(6)			

FIG. 4. The spatial correlation function $G_2(r)$ vs r averaged over 10 burns of the 70 gm^{-2} (○) and 6 burns of the 80 gm^{-2} copier paper (□), and 32 burns of the 9.1 gm^{-2} lens paper (⋆). The crossover lengths r_c are 5.2(1), 7.9(2), and 11.1(1) mm for these paper grades, respectively, shown with vertical lines, and the solid lines indicate slopes that correspond to the exponents in Table I. The curves have been shifted for clarity.
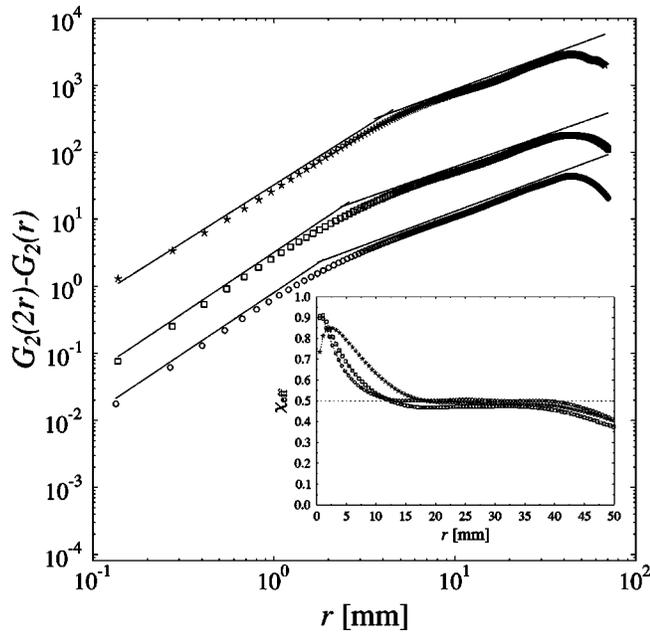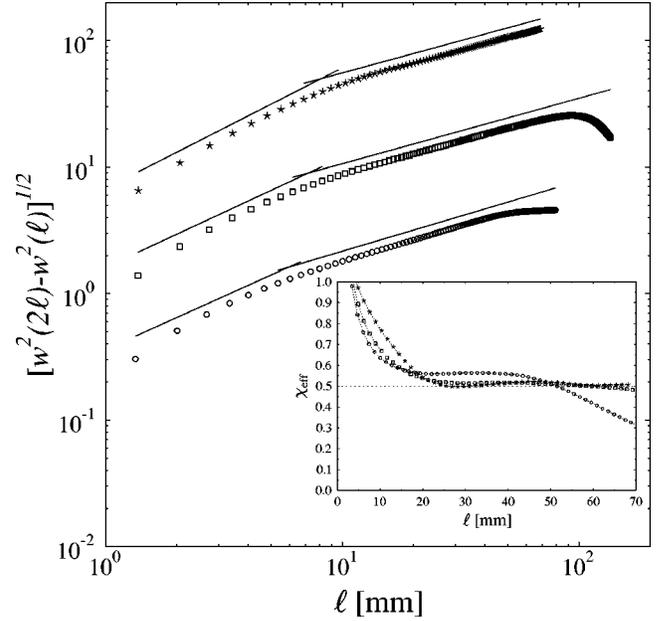

FIG. 6. The local width after the intrinsic width was subtracted $[w^2(2\ell)-w^2(\ell)]^{1/2}$ vs ℓ averaged over 11 burns of the 70 gm^{-2} (○) and 18 burns of the 80 gm^{-2} copier paper (□), and 24 burns of the 9.1 gm^{-2} lens paper (⋆). Solid lines indicate slopes that correspond to Table II. The curves have been shifted for clarity. Inset shows the effective roughness exponent χ_{eff}.

FIG. 5. The spatial correlation function after the intrinsic width has been subtracted $G_2(2r)-G_2(r)$ vs r averaged over 10 burns of the 70 gm^{-2} (○) and 6 burns of the 80 gm^{-2} copier paper (□), and 32 burns of the 9.1 gm^{-2} lens paper (⋆). The solid lines indicate slopes that correspond to the experiments in Table II. The curves have been shifted for clarity. Inset shows the effective roughness exponent χ_{eff} vs r, where the horizontal line is $\chi=1/2$.
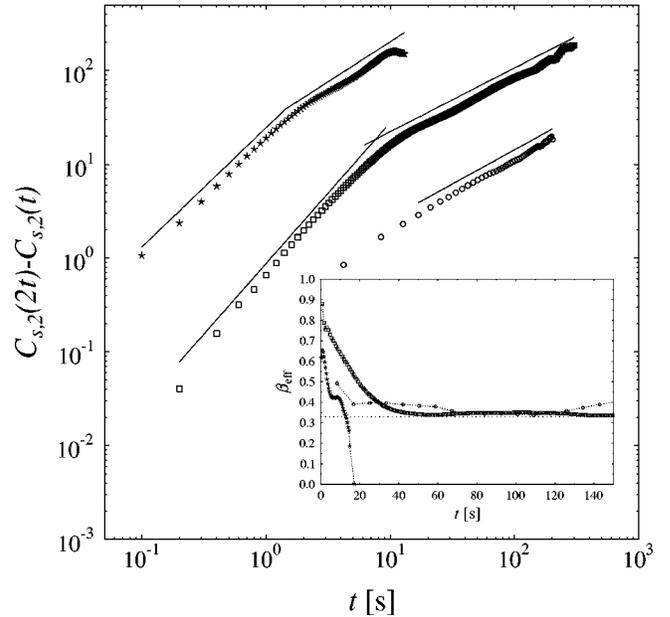

FIG. 7. The temporal correlation function after the intrinsic width was subtracted $C_{s,2}(2t)-C_{s,2}(t)$ vs t averaged over 11 burns of the 70 gm^{-2} (○) and 18 burns of the 80 gm^{-2} copier paper (□), and 24 burns of the 9.1 gm^{-2} lens paper (⋆). The curves have been shifted for clarity. The solid lines indicate slopes that correspond to the experiments in Table II. Inset shows the effective growth exponent β_{eff} vs t. The horizontal line denotes $\beta=1/3$.
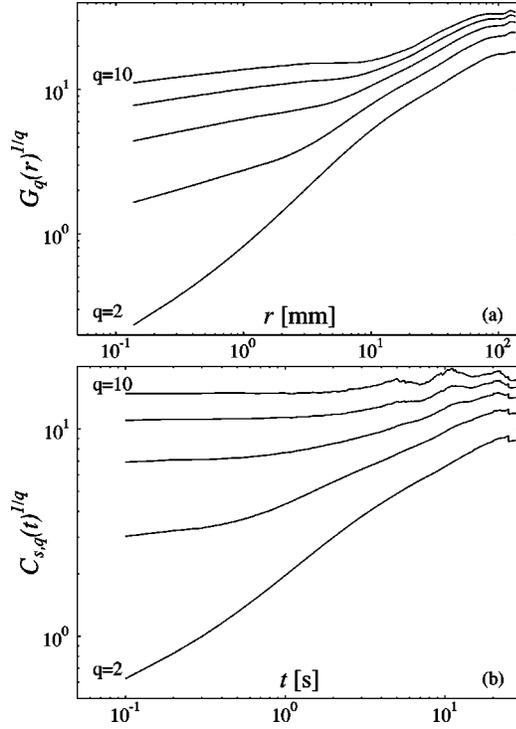
FIG. 8. (a) The qth order spatial correlation function $G_q(r)^{1/q}$ vs r averaged over 32 burns of the 9.1 gm^{-2} lens paper. (b) The qth order temporal correlation function $C_{s,q}(t)^{1/q}$ vs t averaged over 24 burns of the 9.1 gm^{-2} lens paper. The functions in (a) and (b) are plotted for even moments from $q=2$ to 10.

exponents—with some uncertainty as for the higher momenta of the distributions—is very similar for all paper grades, and would thus seem to be a generic feature in these systems. One should however realize that uncorrelated random factors also appear in experiments, which affect the fronts and especially their scaling properties at SR if they involve high gradient values. They are not related to front dynamics and appear therefore as ''artifacts.'' Their effects can be analyzed qualitatively by using standard filtering techniques (e.g., median filtering).

C. Noise correlations

Next we consider the effective noise at the combustion fronts as determined from the fluctuations in the front velocity similar to Ref. [23]. The physics behind this idea is that the presence of local large velocities can be related to the bare noise properties as the maximum front slopes are limited. The effective noise can be analyzed by considering the fluctuations of local velocities, defined as $\delta u(x,t)=u(x,t)-\bar{u}(t)$, with $u(x,t)\equiv(1/\tau)[h(x,t+\tau)-h(x,t)]$, which obviously depend on the timescale τ. Because of the crossover behavior, one has to analyze the noise correlations below ($\tau<t_c$) and above ($\tau>t_c$), the crossover scale. An alternative formulation for the noise amplitude is

$$\eta(x,t)\equiv\delta h(x,t+\tau)-\delta h(x,t), \tag{13}$$

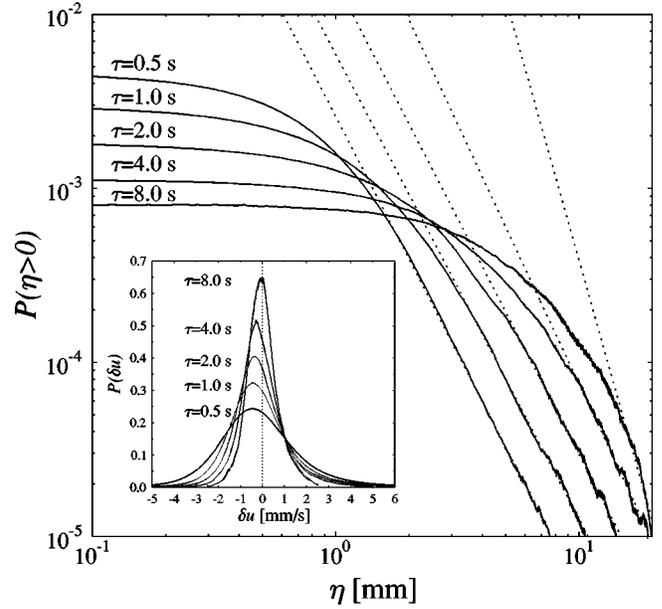where $\delta h=h(x,t)-\bar{h}(t)$. We have used this quantity to estimate the amplitude distribution,

FIG. 9. The noise amplitude distribution $P(\eta>0)$ averaged over 35 burns of the 9.1 gm^{-2} lens paper with an average velocity >8.4 mm/s. The distribution was calculated for time intervals $\tau=0.5$, 1.0, 2.0, 4.0, and 8.0 s shown in the figure. The linear fits have slopes -2.71, -2.67, -2.72, -2.99, and -4.97, left to right. The inset shows the local velocity fluctuation distributions for the same time intervals τ.

$$P(\eta)\equiv\frac{1}{\sum_{\eta'}N(\eta')}N(\eta), \tag{14}$$

in the steady-state regime. Here $N(\eta)$ is the number of positions where η has the same value, and the sum goes over all values of η. We determined $\eta(x,t)$ for time steps $\tau=0.5$, 1.0, 2.0, 4.0, and 8.0 s for the lens paper, and show the related distributions $P(\eta)$ for $\eta>0$ in Fig. 9. For short-time steps the distributions have a good degree of accuracy a power-law tail of the form $P(\eta)=c\,\eta^{-(\mu+1)}$, with $\mu\simeq1.7$. For increasing τ the power-law contribution in the tail of $P(\eta)$ becomes less visible, the exponent μ increases towards $\mu=5$, and the distribution approaches a Gaussian. The behavior is similar to that found for the copier paper [15], except for the exact value of the exponent μ that was found to be about 2.7 at short times ($\tau=1.0$ s).

The local velocity fluctuations were calculated using time steps $\tau=0.5$, 1.0, 2.0, and 4.0 s for the lens paper. In the inset of Fig. 9 we show the corresponding distribution function $P(\delta u)$. For large τ's, $P(\delta u)$ seems to be nearly Gaussian, as expected. For small τ's, it has an asymmetric tail towards higher velocities, which is consistent with nonzero skewness of the TKPZ height distribution [18]. We note that ash formation increases local heat transfer ahead of the combustion front, contributing to this effect in the velocity distribution.

The two-point correlation function of these fluctuations can be expressed in the form
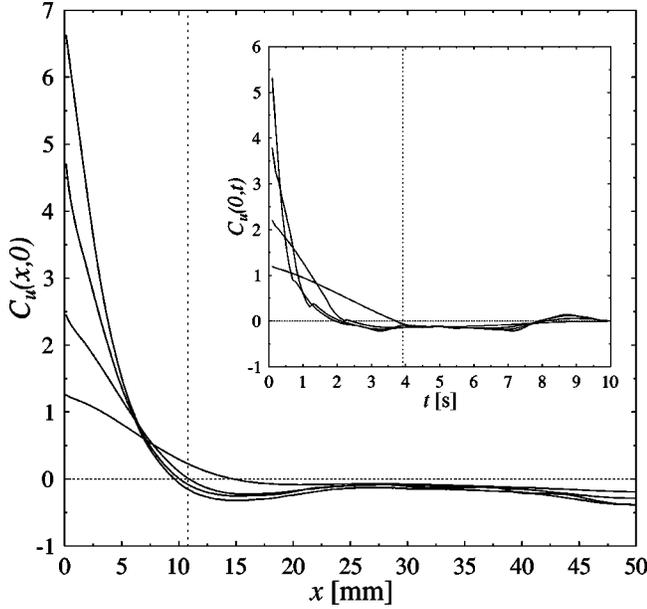
FIG. 10. The spatial and temporal velocity fluctuation correlations $C_u(x,0)$ and $C_u(0,t)$ (inset), respectively, for time intervals $\tau = 0.5$, 1.0, 2.0, and 4.0 s for the 9.1 gm^{-2} lens paper. The crossover length r_c and time t_c (inset) are shown by vertical lines.

$$C_u(x,t) = \langle \delta u(x_0+x,t_0+t)\, \delta u(x_0,t_0) \rangle. \quad (15)$$

This expression is useful for determining possible spatial and temporal correlations. In Fig. 10 we show the spatial correlation functions $C_u(x,0)$ for different time steps τ, and the corresponding temporal correlation functions $C_u(0,t)$ in the inset. The effective spatial and temporal noise was found to be uncorrelated above the crossover scales r_c and t_c, which is in agreement with the TKPZ behavior. Also in this case the behavior of lens paper is analogous to that of the copier papers for which data have been reported in Ref. [15]. Notice that the crossover time is longer than the ratio of the spatial crossover scale and the front velocity would predict.

D. Universal amplitude ratios

We now look at such properties of the TKPZ class as the universal amplitude ratios and the universal coupling constant, discussed in the Introduction. The experimental determination of these quantities is slightly hampered again by the presence of the crossover scales to the TKPZ behavior. Thus the correlation functions and the nonlinearity λ need to be considered in the asymptotic regime only. This means that the available scaling range is limited, but, as we shall see, the results are still in rather good agreement with the theoretical
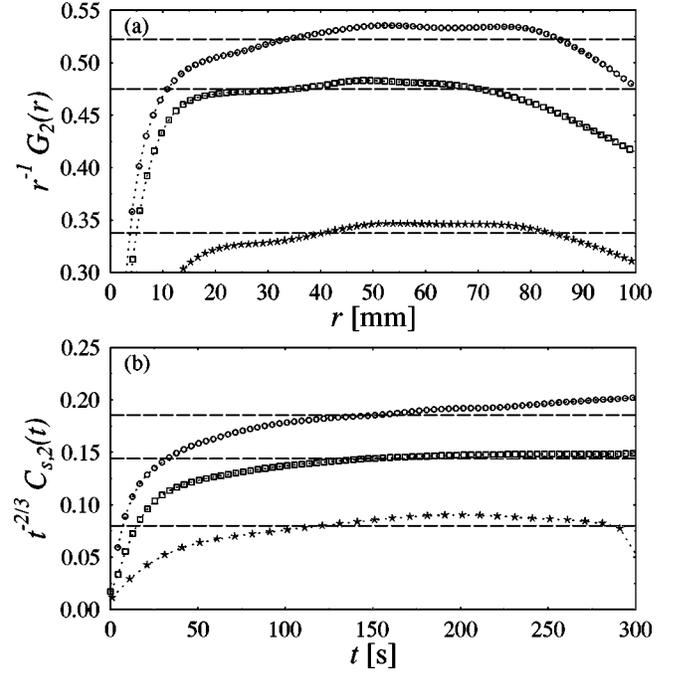

FIG. 11. (a) Measured amplitude of the spatial correlation function $A \equiv r^{-2\chi} G_2(r)$ vs r averaged over 10 burns of the 70 gm^{-2} ($\bigcirc$) and 5 burns of the 80 gm^{-2} copier paper ($\square$), and 32 burns of the 9.1 gm^{-2} lens paper ($\star$) (lens paper data scaled). The horizontal lines indicate the value estimated for A for different paper grades, and it has values 0.54, 0.42, and 3.47, respectively. The roughness exponent was fixed at $\chi = 1/2$. (b) Measured amplitude of the temporal correlation function $B \equiv t^{-2\beta} C_{s,2}(t)$ vs t averaged over 11 burns of the 70 gm^{-2} ($\bigcirc$) and 18 burns of the 80 gm^{-2} copier paper ($\square$), and 24 burns of the 9.1 gm^{-2} lens paper ($\star$) (lens paper data scaled). The horizontal lines indicate the value estimated for B for different paper grades, and it has values 0.18, 0.15, and 9.01, respectively. The growth exponent was fixed at $\beta = 1/3$.

predictions. In any case, correlation functions provide more accurate values for these quantities than the front widths, and we therefore use them here.

We measure from the spatial and temporal correlation functions the prefactors A and B (see the Introduction for a discussion). Figure 11 demonstrates the procedure by which A and B were determined in the saturated TKPZ regime for all three paper grades using reasonable choices for the saturated parts of the correlation functions. The actual values for A, B, and the other parameters are listed in Table III. The amplitude values were augmented by an independent measurement of λ. The interface velocity was determined at each location with a time interval τ long enough to attain the

TABLE III. Results for the correlation amplitudes, λ, and the universal quantities using $\beta = 1/3$ and $\chi = 1/2$.

Paper grade	A	B	λ	R_G	g^*
70 gm^{-2}	0.52(2)	0.186(12)	0.465(2)	0.74(6)	0.79(9)
80 gm^{-2}	0.475(7)	0.14(1)	0.370(1)	0.73(5)	0.76(8)
9.1 gm^{-2}	3.4(1)	8.0(8)	4.0(4)	0.62(8)	1.0(2)

TKPZ regime, with a simultaneous determination of the local interface slope. The velocity vs slope data were then fitted by a parabola using slopes between -0.5 and 0.5 [35], corresponding typically to about a half of all the slopes.

Combining the results for λ, A, and B with the exact TKPZ exponents, we obtain for the coupling constant g^* the values shown in Table III. It is evident from this table that the results are in good agreement with theory, with the largest deviation showing up for the 70-gm^{-2} grade. Recall that the mode-coupling value is $g^* \simeq 0.87$ [8]. If we use the measured exponents instead, g^* becomes 0.8(2), 0.8(2), and 2.7(4) for the 70-gm^{-2}, 80-gm^{-2}, and 9.1-gm^{-2} grades, respectively. The last value is due to the large effective β for the lens paper, caused by the very short saturated regime, and thereby poor statistics in the temporal correlation function. The same quantities, λ, A, B, and the TKPZ exponents, also define the universal amplitude ratio R_G, whose measured values are also shown in Table III. As the mode-coupling and simulation results for R_G vary in the range $R_G = 0.63$–0.71, agreement with theoretical predictions is good also in this case. Notice that g^* and R_G are functionally related when the exact TKPZ exponents are used in their expressions.

The local width $w(\ell, t)$ allows, furthermore, for the determination of a scaling function related to that of Eq. (2). One can show, see e.g. [10,11], that $w(\ell, t) = C_\ell \ell^\chi F(|\lambda| C_\ell t / \ell^z)$, where C_ℓ is determined by the asymptotic value (at $t = \infty$) of w, $w(\ell) = C_\ell \ell^\chi$. Using a maximum value of $\ell \simeq 14$ cm, and fitting the C_ℓ values for the three grades, one can collapse the time-dependent data with the aid of the λ values as measured from the slope-dependent local velocities of the fronts [10,11]. The result is shown in Fig. 12. As the measured λ and C_ℓ values are not very accurate, we show in the inset of this figure the best collapse of the data achieved by using C_ℓ essentially as a free parameter.

V. DISCUSSION AND CONCLUSIONS

In this paper we have made a thorough survey and analysis of our experiments on kinetic roughening of slow-combustion fronts in paper. The general conclusion is that well-controlled experiments lead to a clear asymptotic scaling that is unequivocally in accord with the thermal KPZ universality class. This is evident from the asymptotic behavior of the qth order correlation functions, and from the scaling exponents determined from them, as well as from independent measurements using the local width. We also augment the evidence by computing a universal amplitude ratio characterizing the TKPZ universality class, and the universal (KPZ fixed-point) coupling constant, and find good agreement with theoretical estimates.

In the analysis of our experimental results it proved to be of crucial importance to do extensive averaging over independent slow-combustion fronts. Fluctuations in the noise affecting the fronts give rise to wide fluctuations in individual fronts, also from burn to burn. There is quenched noise due to density variations typical of paperlike materials, and the effective noise also includes dynamical effects. A
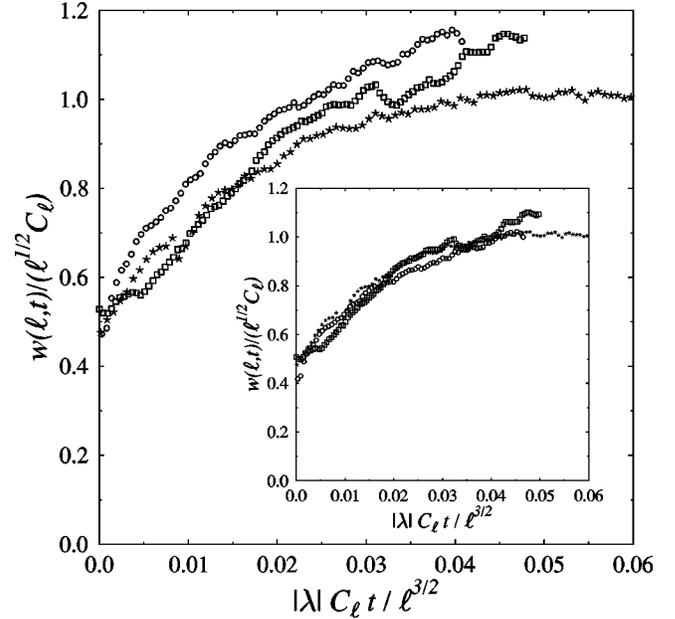

FIG. 12. Scaling plots for $w(\ell, t) = \ell^{1/2} C_\ell F(|\lambda| C_\ell t / \ell^{3/2})$ averaged over 39 burns of the 70 gm^{-2} ($\bigcirc$) and 34 burns of the 80 gm^{-2} copier paper ($\square$), and 24 burns of the 9.1 gm^{-2} lens paper ($\star$). The inset shows the best collapse of these data, achieved by letting C_ℓ vary (a variation within a few percent was enough) as a free parameter.

burning front creates around it a fluctuating flow of air, and this flow will give rise to fluctuations in the "effective" heat conductivity (due to convective transfer of heat) and in cooling. These dynamical fluctuations could be demonstrated by adjusting the overall air flow in the combustion chamber, and thereby regulating the crossover scales parallel to the flow. The temporal crossover scales are always clearly longer than the spatial crossover scales along the fronts divided by the average front velocities. This is indicative of dynamical convective effects. We found that averaging over approximately ten independent burns is needed for fairly reliable estimates for the quantities measured. For copier paper this means in practice averaging over about 40 000 individual fronts, and for lens paper, with much faster propagating fronts, over several thousand individual fronts. For the lens paper, averaging was hampered by the shortness of the saturated regime.

In addition to the demonstration of the asymptotic TKPZ behavior, another interesting feature is the persistent crossover present in slow combustion of paper. The apparent scaling properties of the fronts are markedly different at short time and length scales as compared to the asymptotics. This phenomenon was first observed [24] in fluid-flow experiments, and very recently also in [25] penetrating flux fronts in thin-film superconductors. As discussed in the Introduction, several possible mechanisms have been suggested for this phenomenon (see also Ref. [2] for a review). Before our work, the reasons and consequences of the two regimes was not settled experimentally though power-law distributed amplitudes in the effective noise were reported both in [23] for fluid-flow experiments and in [15] for slow combustion of paper. In the latter experiments, performed by us, noise cor-

relations were furthermore found to be short ranged, both in space and in time. Moreover, the ''decay lengths'' of these correlations seem roughly to coincide with the crossover scales in the height-height correlation functions. It thus appears that the SR correlations in the noise affecting the fronts, either quenched or annealed, or both, are likely to be responsible for the crossovers and the related higher apparent exponents at short range. The continuous decay of SR correlations would also explain the lack of true scaling in that regime, i.e., the running exponents do not show plateaux there. In the case of slow combustion of paper at least, the effective noise clearly is part of a dynamical origin. Thus quenched noise alone cannot be decisive for the short-range effects, although it leads to a similar crossover behavior. Our measured SR exponents shown in Table II do not agree with the apparent SR exponents for moving fronts with quenched noise: close to the depinning transition $\beta \simeq \chi \simeq 0.75$ [19]. Some effects at SR due to the irrelevant terms in the appropriate Langevin equation cannot, of course, be ruled out.

Multiscaling at short range seems, on the other hand, to result from other features in the fronts. It is evident that regions of high gradient (in absolute value) are amplified in the higher-order correlation functions, and thereby affect the multiscaling properties of the fronts. Distinct regions of such high gradient values appear if successive fronts are plotted as surface diagrams. Note that digitizing errors, and sharp natural defects in the observed data, also make a contribution to the apparent multiscaling properties, and should be filtered out as artifacts. Fairly sharp steps, which occasionally appear in the (filtered) fronts, also begin to move also sideways, driven by the nonlinear term in the KPZ equation Eq. (1). These moving structures appear as local ''avalanches'' in the propagating fronts. By analyzing distinct intervals of propagating combustions fronts, containing varying amounts of such avalanches, we can conclude that the q dependence at SR of the slopes of the spatial and temporal correlation functions extend longer when there are more avalanches present. This effect is however difficult to quantify precisely as it is neither possible to completely remove the avalanches, nor the experimental artifacts, from real data.

We have only considered here well-propagating fronts in which pinning effects do not appear. By reducing the KNO_3 concentration, we can however approach the pinning regime in a rather controlled way. A lot of statistics must be produced again, since the exact amount of KNO_3 absorbed in the paper samples (the ''driving force'') is difficult to regulate. Nevertheless, in this way we think one can eventually determine the interface behavior also at pinning. It is evident that there will also be crossovers present in this case, with the actual crossover scales probably depending on the driving force.

---

[1] A.-L. Barabási and H. E. Stanley, *Fractal Concepts in Surface Growth* (Cambridge University Press, Cambridge, 1995).

[2] T. Halpin-Healy and Y.-C. Zhang, Phys. Rep. **254**, 215 (1995).

[3] P. Meakin, *Fractals, Scaling and Growth Far From Equilibrium* (Cambridge University Press, Cambridge, 1998).

[4] M. Kardar, G. Parisi, and Y.-C. Zhang, Phys. Rev. Lett. **56**, 889 (1986).

[5] F. Family and T. Vicsek, J. Phys. A **18**, L75 (1985).

[6] D. Forster, D. Nelson, and M. Stephen, Phys. Rev. A **16**, 732 (1977).

[7] E. Medina, T. Hwa, M. Kardar, and Y.-C. Zhang, Phys. Rev. A **39**, 3053 (1989).

[8] T. Hwa and E. Frey, Phys. Rev. A **44**, R7873 (1991).

[9] H. Fogedby, Phys. Rev. E **57**, 4943 (1998).

[10] J. G. Amar and F. Family, Phys. Rev. A **45**, R3373 (1992).

[11] J. G. Amar and F. Family, Phys. Rev. A **45**, 5378 (1992).

[12] J. Krug, P. Meakin, and T. Halpin-Healy, Phys. Rev. A **45**, 638 (1992).

[13] E. Frey, U. C. Täuber, and T. Hwa, Phys. Rev. E **53**, 4424 (1996).

[14] J. Maunuksela, M. Myllys, O.-P. Kähkönen, J. Timonen, N. Provatas, M. Alava, and T. Ala-Nissila, Phys. Rev. Lett. **79**, 1515 (1997).

[15] M. Myllys, J. Maunuksela, M. Alava, T. Ala-Nissila, and J. Timonen, Phys. Rev. Lett. **84**, 1946 (2000).

[16] J. Zhang, Y.-C. Zhang, P. Alstrom, and M. Levinsen, Physica A **189**, 383 (1992).

[17] K. Sneppen *et al.*, Phys. Rev. A **46**, R7351 (1992); F. Hayot, C. Jayaprakash, and Ch. Josserand, Phys. Rev. E **47**, 911 (1993).

[18] J. Neergaard and M. den Jijs, J. Phys. A **30**, 1935 (1997).

[19] H. Leschhorn, Phys. Rev. E **54**, 1313 (1996).

[20] M.-P. Kuittu, M. Haataja, and T. Ala-Nissila, Phys. Rev. E **59**, 2677 (1999).

[21] A.-L. Barabási, R. Boubonnais, M. Jensen, J. Kertesz, T. Vicsek, and Y.-C. Zhang, Phys. Rev. A **45**, R6951 (1992).

[22] M. Dubá *et al.*, Phys. Rev. Lett. **83**, 1628 (1999); Eur. Phys. J. B **15**, 701 (2000); **15**, 691 (2000).

[23] V. Horváth, F. Family, and T. Vicsek, Phys. Rev. Lett. **67**, 3207 (1991).

[24] V. Horváth, F. Family, and T. Vicsek, J. Phys. A **24**, L25 (1991).

[25] R. Surdeanu, R. J. Wijngaarden, E. Vissar, J. M. Huijbregtse, J. H. Rector, B. Dam, and R. Griessen, Phys. Rev. Lett. **83**, 2054 (1999).

[26] The 70 gm^{-2} copier paper (KymLux) was manufactured by UPM-Kymmene, Finland. The 80 gm^{-2} copier paper was manufactured by Metsä-Serla at Kangas Paper Mill, Finland. The 9.1 gm^{-2} lens paper was manufactured by Whatman Paper Ltd., U.K.

[27] N. Provatas, M. Alava, and T. Ala-Nissila, Phys. Rev. E **54**, R36 (1996).

[28] L.-H. Tang and H. Leschhorn, Phys. Rev. A **45**, R8309 (1992).

[29] H. J. Häkkänen and J. E. I. Korppi-Tommola, Appl. Spectrosc. **49**, 1721 (1995).

[30] D. Wolf and J. Kertesz, J. Phys. A **20**, L257 (1987).

[31] J. Kertész and D. Wolf, J. Phys. A **21**, 747 (1988).

[32] B. M. Forrest and L.-H. Tang, Phys. Rev. Lett. **64**, 1405 (1990).

[33] A.-L. Barabási, P. Szepfalusy, and T. Vicsek, Physica A **178**, 17 (1991).

[34] A.-L. Barabási and T. Vicsek, Phys. Rev. A **44**, 2730 (1991).

[35] R. Albert, A.-L. Barabási, N. Carle, and A. Dougherty, Phys. Rev. Lett. **81**, 2926 (1998).